materials

MDPI

Article

Intrinsic Properties of Multi-Layer $TiO_2/V_2O_5/TiO_2$ Coatings Prepared via E-Beam Evaporation

Irfa Rehman [1,†], Muhammad Bilal Hanif [2,†], Abdulaziz Salem Alghamdi [3], Abdul Khaliq [3], K. S. Abdel Halim [3,4], Tayyab Subhani [3,*], Martin Motola [2,*] and Abdul Faheem Khan [1,*]

1 Department of Materials Science and Engineering, Institute of Space Technology, 1-National Highway, Islamabad 44000, Pakistan; effiaffi92@gmail.com
2 Department of Inorganic Chemistry, Faculty of Natural Sciences, Comenius University in Bratislava, Ilkovicova 6, Mlynska Dolina, 842 15 Bratislava, Slovakia; hanif1@uniba.sk
3 College of Engineering, University of Ha'il, Ha'il P.O. Box 2440, Saudi Arabia; a.alghamdi@uoh.edu.sa (A.S.A.); ab.ismail@uoh.edu.sa (A.K.); k.abdulhalem@uoh.edu.sa (K.S.A.H.)
4 Central Metallurgical Research and Development Institute (CMRDI), P.O. Box 87, Helwan 11421, Egypt
* Correspondence: ta.subhani@uoh.edu.sa (T.S.); martin.motola@uniba.sk (M.M.); afkhan_ist@yahoo.com or abdul.faheem@ist.edu.pk (A.F.K.)
† These authors contributed equally to this work.

Abstract: Nanocomposite multi-layer $TiO_2/V_2O_5/TiO_2$ thin films were prepared via electron-beam evaporation using high-purity targets (TiO_2 and V_2O_5 purity > 99.9%) at substrate temperatures of 270 °C (TiO_2) and 25 °C (V_2O_5) under a partial pressure of oxygen of 2×10^{-4} mbar to maintain the stoichiometry. Rutherford backscattering spectrometry was used to confirm the layer structure and the optimal stoichiometry of the thin films, with a particle size of 20 to 40 nm. The thin films showed an optical transmittance of ~78% in the visible region and a reflectance of ~90% in the infrared. A decrease in transmittance was observed due to the greater cumulative thickness of the three layers and multiple reflections at the interface of the layers. The optical bandgap of the TiO_2 mono-layer was ~3.49 eV, whereas that of the multi-layer $TiO_2/V_2O_5/TiO_2$ reached ~3.51 eV. The increase in the optical bandgap was due to the inter-diffusion of the layers at an elevated substrate temperature during the deposition. The intrinsic, structural, and morphological features of the $TiO_2/V_2O_5/TiO_2$ thin films suggest their efficient use as a solar water heater system.

Keywords: TiO_2; V_2O_5; multi-layer; thin films; Rutherford backscattering (RBS); solar water heater

Citation: Rehman, I.; Hanif, M.B.; Alghamdi, A.S.; Khaliq, A.; Halim, K.S.A.; Subhani, T.; Motola, M.; Khan, A.F. Intrinsic Properties of Multi-Layer $TiO_2/V_2O_5/TiO_2$ Coatings Prepared via E-Beam Evaporation. *Materials* **2022**, *15*, 3933. https://doi.org/10.3390/ma15113933

Academic Editor: Dong-Joo Kim

Received: 25 April 2022
Accepted: 29 May 2022
Published: 31 May 2022

1. Introduction

Economic growth and the everyday activities of human life are dependent on energy. However, the depletion of fossil fuels and environmental factors such as global warming have made the energy crisis of paramount importance, necessitating a search for more dependable means to fulfill energy requirements. The technology for harvesting renewable energy is still being developed, as it has not yet reached the required standard. As solar energy is a prominent source of renewable energy, the aim of this paper is to improve the efficiency of energy-harvesting devices. Solar energy can be converted into electrical and thermal energy via the photovoltaic effect, and materials based on this phenomenon are now used in solar cells and solar heaters [1]. The efficient utilization of incident light is crucial for a photovoltaic cell's performance, i.e., the generation of the charge carriers (e^-/h^+). The photogenerated charge carriers are subsequently transported to the electrodes that facilitate the flow of e^-/h^+, converting them to current. Such energy is currently used in industrial and domestic facilities (the operation of machinery, air conditioning, and lighting) [2]. In the case of solar heaters, the incident photons are converted to useable heat via the so-called solar–thermal energy conversion. In solar–thermal devices, the photonic radiation is converted to phononic vibration in the absorber, which is then transported to

the desired location using a carrier material (e.g., water). The applications of this process include space heating, industrial processes (generation of heat), air conditioning, water heating, drying, desalination, distillation, and electrical energy generation [3,4].

Three crucial intrinsic properties of a solar water heater device (SWHD) are required to maximize its efficiency: (1) good thermal conduction, (2) incident light utilization, and (3) high transmittance [5,6]. In addition, low-reflective materials are important for efficient SWHDs, as reflected incident light is considered a loss in terms of energy, thus decreasing the performance of SWHDs [7]. Moreover, SWHDs generate temperatures of up to 1000 °C; thus, high thermal stability is essential [4].

Vanadium oxide (V_2O_5) is a chromogenic material that has been studied extensively due to its unique photoelectrochemical properties [8–10]; nowadays, it is used in energy-efficient smart windows [11]. Bulk V_2O_5 undergoes a semiconductor-to-metallic phase transition at 257 °C, possessing an orthorhombic structure with an indirect bandgap of 2.6 eV [12,13]. At high temperatures (>Tc), the metal-like V_2O_5 possesses a different crystal structure compared to that at low temperatures. At room temperature, it possesses an orthorhombic structure which transforms to a metastable monoclinic structure at around 450 °C [14]. Nevertheless, Kang M. et al. [15] reported V_2O_5 thin films without any crystal structure or phase transition changes during the insulator-to-metal transition of V_2O_5. Indeed, the phase transition corresponds to a change in the electrical conductivity (with changes of up to 10 orders of magnitude), whereas discontinuity can be seen for the optical and magnetic properties of V_2O_5 [16].

The solar water heater system proposed in this study constitutes multi-layer TiO_2 and V_2O_5 thin films. V_2O_5 has variable optical properties and thus has been used in diverse technological applications such as infrared (IR) detectors, memory devices, smart windows, artificial muscles, electronic information displays, lithium batteries, and optical and electrical switches [17–23]. There are several oxides of vanadium, each with stability over a particular composition range. The thin films of vanadium pentoxide show a refractive index of 1.9–2.09 [24], with a bandgap value range of 2.04–3.25 eV [24–27]. This high refractive index is associated with good transparency in the visible region.

The bandgap of TiO_2 is wide, and thus it finds its way into various applications, including photocatalysis, optical fibers, photo electrolysis, biomedical processes, and photovoltaics [15,28–30]. TiO_2 has been diversely employed in solar devices in the form of cathodes, light scatterers, electron collectors, high wavelength transmitters, etc. These applications are possible due to its tunable conductivity, resistance to weathering, self-cleaning ability, excellent transmittance of solar radiation, and ease of fabrication [31–47]. TiO_2 has been utilized in the form of a mesoporous nanostructure to increase scattering, which increases the interaction of light with absorbing materials and eventually improves the absorption efficiency [31]. The three crystalline forms of TiO_2 have different crystal structures, and thus their optical properties also differ [32]. The anatase phase of TiO_2 thin films is promising for applications in optics because of its high transparency in the visible region and its high reflective index [33]. Furthermore, V_2O_5 films along with TiO_2 have been prepared using the electron beam evaporation technique due to its cost-effectiveness, easy control of parameters, uniformity, and stoichiometry, which is still a challenge in other PVD fabricated films. However, the stoichiometry of the system can be controlled easily by the annealing process. Comparatively, sputtering, atomic layer deposition, and molecular beam epitaxy produce more stoichiometric films than the e-beam technique; however, these are expensive techniques and ultimately increase the cost of the whole system. An additional advantage of the e-beam technique is that we can achieve a higher deposition rate without affecting the uniformity and stoichiometry of the films.

In the present work, we prepared SWHDs based on a nanocomposite $TiO_2/V_2O_5/TiO_2$ multi-layer thin film via e-beam evaporation [48,49], consisting of a ~50 nm-thick V_2O_5 layer sandwiched between two TiO_2 layers (a ~100 nm-thick bottom layer and a ~360 nm-thick upper layer) on a transparent 1 mm-thick soda–lime glass (as depicted in the graphical abstract). A comprehensive characterization of the intrinsic properties of the $TiO_2/V_2O_5/TiO_2$

SWHD was conducted using X-ray diffractometry (XRD), scanning electron microscopy (SEM), energy-dispersive X-ray spectroscopy (EDS), Rutherford backscattering spectrometry (RBS), atomic force microscopy, and transmittance spectra (TS). The prepared TiO_2/V_2O_5/TiO_2 thin film possessed suitable properties for potential application in solar-to-heat conversion, i.e., SWHDs.

2. Experimentation

TiO_2 (purity > 99.99%) and V_2O_5 (purity > 99.9%) powders were used as starting materials, which were converted to pellets using polyvinyl gel (PVA) as a binder. Briefly, 2.5 g of PVA gel was dissolved in 100 mL of DI H_2O. Afterward, the solution (binder) was heated to 200 °C and stirred for 3 h. The binder solution was subsequently used for the preparation of 10 mm-thick pellets by applying a 799.934 mbar hydraulic press.

A nanocomposite TiO_2/V_2O_5/TiO_2 multi-layer thin film was fabricated using the electron beam (e-beam) evaporation technique. The deposition was performed under a vacuum of 1×10^{-5} mbar and the partial pressure of oxygen was kept to 2×10^{-4} mbar during the deposition of TiO_2 (deposition rate ~0.45 nm/s) and V_2O_5 (deposition rate ~0.15 nm/s) to maintain the stoichiometry of the layers. The first layer of TiO_2 (~100 nm thickness) was deposited on a soda–lime glass substrate at a substrate temperature of 270 °C. Subsequently, the second layer of V_2O_5 (~50 nm thickness) was deposited at a substrate temperature of 25 °C. Lastly, the third layer of TiO_2 (~360 nm thickness) was deposited at a substrate temperature of 270 °C (the device is visualized in the graphical abstract). To distinguish the different layered structures, we refer to them as follows: (i) mono-layer, i.e., 100 nm-thick TiO_2; (ii) bi-layer, i.e., 50 nm-thick V_2O_5 on 100 nm-thick TiO_2; and (iii) tri-layer, i.e., 360 nm-thick TiO_2 on 50 nm-thick V_2O_5 on 100 nm-thick TiO_2.

The stoichiometric analysis and the thickness of each layer was measured with Rutherford backscattering spectroscopy (RBS) using a 2MeV Pelletron Tandem Accelerator (5UDH-2 Pelletron). The mean energy used for the RBS analysis was 2 MeV (He^{2+} beam). The incident and scattering angles were 70° and 170°, respectively. Cornell geometry was used for the measurements, with a constant angle of 170° and 13 cm of distance between the sample and the detector. The simulation software SIMNRA was used for the data analysis.

Field-emission scanning electron microscopy (FESEM, MIRA3 TESCAN) and energy-dispersive X-ray spectroscopy (EDS) were used to determine the surface morphology, topography, and elemental properties of the films.

An X-ray diffractometer (XRD, PANalytical, Cu Ka radiation, λ = 1.5418 Å) was used to study the crystal structure of the nanocomposite at room temperature.

To obtain deeper insight into the influences of the surface roughness and skewness on the different TiO_2 nanostructures, atomic force microscopy (AFM, Quesant Universal SPM, Ambios Technology) was conducted in contact mode using standard silicon AFM probes.

The electrical resistivity of the film was analyzed using a DC-4-point probe method at 25 °C.

Optical transmittance was measured at 25 °C by a Perkin Elmer UV/VIS/NIR Lambda 19 spectrophotometer in the wavelength range of 250–2500 nm.

3. Results and Discussion

First, a step-by-step FESEM analysis (layer-by-layer) was conducted to determine the surface morphology of our SWHD. The top views of the mono-, bi-, and tri-layers are depicted in Figure 1a–c. In general, the surfaces of all the layers showed dense, smooth structures with good uniformity, i.e., no cracks or peel-offs were present. At higher magnifications of the tri-layer (Figure 1d), a nanocomposite surface was observed with a clear nanoparticle-like structure and a particle size in the range of 20–40 nm. The quality of the film improved with an increase in the substrate temperature during deposition, as there was an adequate amount of energy for atoms to be arranged uniformly.

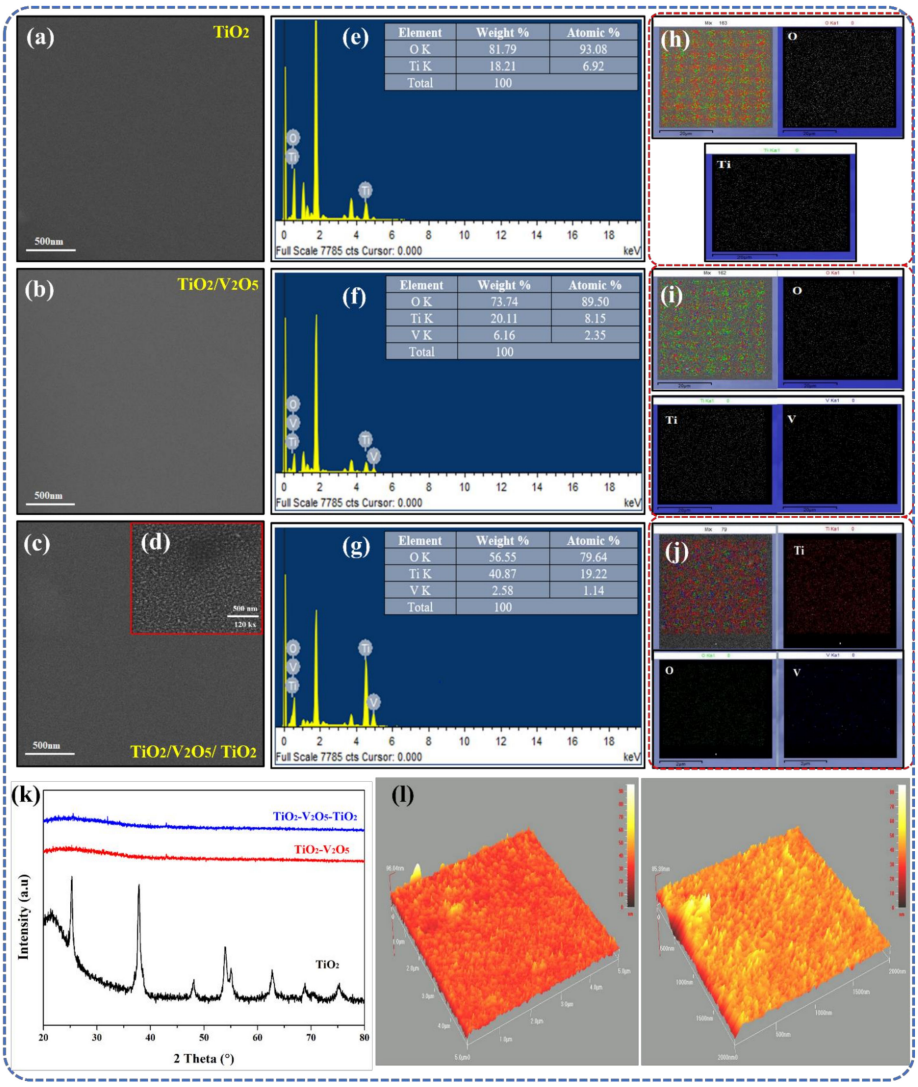

Figure 1. Surface morphology of (**a**) TiO_2, (**b**) TiO_2/V_2O_5, and (**c**) $TiO_2/V_2O_5/TiO_2$ at 80 kx magnification and (**d**) $TiO_2/V_2O_5/TiO_2$ at 120 kx magnification. EDS analysis and elemental area mapping of (**e**,**h**) single-layer TiO_2, (**f**,**i**) bi-layer TiO_2/V_2O_5, and (**g**,**j**) multi-layer $TiO_2/V_2O_5/TiO_2$ thin film. (**k**) XRD analysis of single-, bi-, and tri-layer thin films. (**l**) AFM topography of a multi-layer $TiO_2/V_2O_5/TiO_2$ thin film on 2×2 μm^2 and 5×5 μm^2, respectively.

EDS mapping was conducted to determine the presence and distribution of elements across the whole surface. The results are summarized in Table 1. The energy dispersive X-ray spectroscopic (EDS) analysis of the single-layer TiO_2_ film is shown in Figure 1e. EDS revealed the presence of Ti atoms in the film. The glass substrate contributed to the excessive oxygen in the films. Figure 1f shows the EDS analysis of the TiO_2/V_2O_5 bi-layer film, which revealed the presence of vanadium atoms alongside the Ti atoms, indicating the development of the TiO_2/V_2O_5 bi-layer film. The EDS analysis of the $TiO_2/V_2O_5/TiO_2$ tri-layer film is shown in Figure 1g. The Ti atoms are present in greater amounts than in the EDS results in Figure 1e,f, indicating the formation of the $TiO_2/V_2O_5/TiO_2$ tri-layer film.

Table 1. Concentrations of mono-, bi-, and tri-layers as determined by RBS and EDS, and intended and determined thicknesses of the individual layers.

No. of Layers	Mono-Layer (TiO_2)	Bi-Layer (TiO_2/V_2O_5)	Tri-Layer ($TiO_2/V_2O_5/TiO_2$)
Concentration determined by RBS	Ti:30 O:70	Ti:18 V:8 O:74	Ti:35 V: 5 O:60
Intended thickness (nm)	100	50	360
Calculated thickness (nm)	150	54	400
Concentration determined by EDS (wt.%)	Ti:18 O:82	Ti:20 O:74 V:6	Ti:42 O:56 V:2

Elemental area mapping was also performed to confirm the results of EDS. These results are shown in Figure 1h–j, and the relative decrease in oxygen atoms due to the addition of V and Ti atoms is depicted in Figure 1i,j. The deposition and dispersion of single-layer, bi-layer, and multi-layer thin films were uniform throughout the surface, as characterized by the results of the elemental area mapping. Overall, the EDS results corresponded well with those of the elemental area mapping, indicating that the $TiO_2/V_2O_5/TiO_2$ tri-layer film was effectively fabricated.

As reported [4], a high thermal stability (up to 1000 °C) is necessary for a material to be potentially used as a SWHD. Thus, a simple test was conducted in order to evaluate the thermal stability of our $TiO_2/V_2O_5/TiO_2$ tri-layer film. The sample was put in a muffle oven and heated up to 1000 °C for 3 h. No cracks were visible on the surface of the $TiO_2/V_2O_5/TiO_2$ tri-layer film, indicating that a good thermal stability was achieved.

Figure 1k shows the XRD patterns for the mono-, bi-, and tri-layers. In the case of the TiO_2 mono-layer, only one crystal structure was identified: tetragonal anatase TiO_2 (space group $P4_2/mnm$, ICCD 01-086-1157) [50]. After depositing an additional layer (V_2O_5 in the bi-layer and V_2O_5/TiO_2 in the tri-layer), the amorphous nature of the thin film was identified. Using the Scherer formula, the crystallite size was determined to be 23.5 nm for the single-layer TiO_2 film. As previously reported, this is a well-known behavior of such thin films [51,52]. All in all, the proposed tri-layer thin film is suitable for use as a SWHD due to its promising surface morphology and crystal structure.

Additional information about the surface morphology alterations of the $TiO_2/V_2O_5/TiO_2$ tri-layer film was acquired using AFM (Figure 1l) The relevant nanoscale roughness was determined on areas of 2×2 μm^2 and 5×5 μm^2, respectively. Such AFM scans are considered representative and are beneficial for studying the surfaces of thin films [51]. Furthermore, surface roughness also describes the light scattering along with the quality of the surface under investigation. The surface of the $TiO_2/V_2O_5/TiO_2$ tri-layer film was observed to have no cracks and to be rather smooth (with low roughness values), which is necessary for the thin film to be considered for application as a SWHD.

The RBS spectra of the mono-, bi-, and tri-layers are shown in Figure 2a–c. Only one peak was observed in the mono-layer (Figure 2a), which confirms the presence of TiO_2 and the thickness (150 nm) of the layer, with a Ti:O atomic ratio of 30%:70%. The RBS spectra of the bi-layer (Figure 2b) showed two peaks representing Ti (Ti 30%: O_2 70%) and V (V 12%: O_2 88%), respectively. The kinematic factors for Ti and V are 0.7166 and 0.7313, respectively; thus, the diffusion of the peaks was observed [34,35]. The RBS spectra of the tri-layer (the final concept of our SWHD) showed one peak for V and two peaks for Ti. The 100 nm-thick bottom TiO_2 layer was observed at a higher channel (I_{max} ~ 1100 channel) compared to that of the 360 nm-thick top TiO_2 layer (I_{max} ~ 1000 channel). The position of the I_{max} was kinematic factor-dependent, i.e., the lower TiO_2 layer appeared at a higher channel. The 50 nm-thick V_2O_5 layer (I_{max} ~ 1250 channel) was sandwiched between the two TiO_2 layers. The RBS data confirmed the formation of a multi-layered structure within the tri-layer, with

optimal stoichiometry and film thickness (Table 1). The calculated thicknesses of the layers differ from the intended (theoretical) ones as follows: (i) 150 nm-thick bottom TiO_2 layer (theoretical: 100 nm); (ii) 54 nm-thick V_2O_5 layer (theoretical: 50 nm); and (iii) 400 nm-thick top TiO_2 layer (theoretical: 360 nm). The following equation was used to determine the thicknesses of the layers via RBS, where the total energy loss (ΔE) is proportional to the depth (t). With this approximation, the relationship between the energy width ΔE of the signal from the thickness of the film (Δt) can be derived:

$$\Delta E = \Delta t \left(k \frac{dE}{dx_{in}} + \frac{1}{cos\theta} \frac{dE}{dx_{out}} \right)$$

where θ is the lab scattering angle, k is the kinematic factor, and x_{in} and x_{out} indicate the energies at which the rate of energy loss is evaluated.

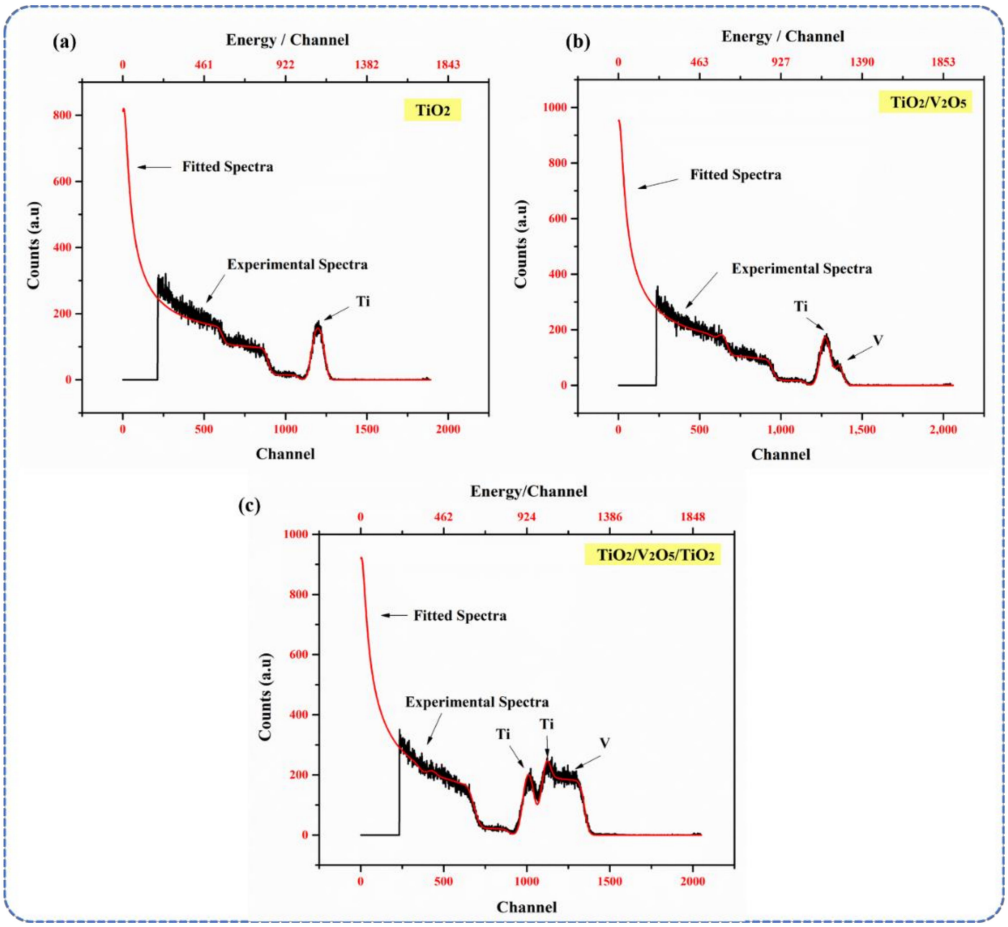

Figure 2. RBS spectra of (**a**) mono-layer TiO_2, (**b**) bi-layer TiO_2/V_2O_5, and (**c**) multi-layer TiO_2/V_2O_5 thin films, respectively.

The optical properties (in particular, transmittance and the optical bandgap) of a material are crucial for determining its potential use as a solar water heater. The transmittance spectra of mono-, bi-, and tri-layers are shown in Figure 3 from 250 nm to 2500 nm. A transmittance of ~92%, ~82%, and ~78% was achieved in mono-, bi-, and tri-layers in the visible range, respectively, as shown in Figure 3a–d. The high transmittance for the mono-layer was due to its thinner overall film thickness compared to that of the bi- and tri-layers. After the deposition of the 50 nm-thick V_2O_5 layer (in the bi-layer), a substantial decrease of 10% was observed. This occurred because, as reported [37], the optical absorption edge of V_2O_5 thin films appears in the wavelength range from 400 nm to 500 nm (A_{max} = 390 nm; A_{min} = 330 nm). Thus, the absorption properties of V_2O_5 are relatively low at wavelengths > 500 nm. Moreover, the increased total thickness of the bi-layer (~200 nm)

compared to that of the mono-layer (~150 nm) resulted in the decreased absorption of incident light. In the tri-layer, the decrease in the transmittance was two-fold due to: (i) an increase in the total thickness of the thin film (~600 nm) compared to the mono- and bi-layer thin films, and (ii) multiple incident photon reflections at the interface between the different $TiO_2/V_2O_5/TiO_2$/glass layers. In addition, a shift into the red region was present in the tri-layer due to the increased thickness of the thin film.

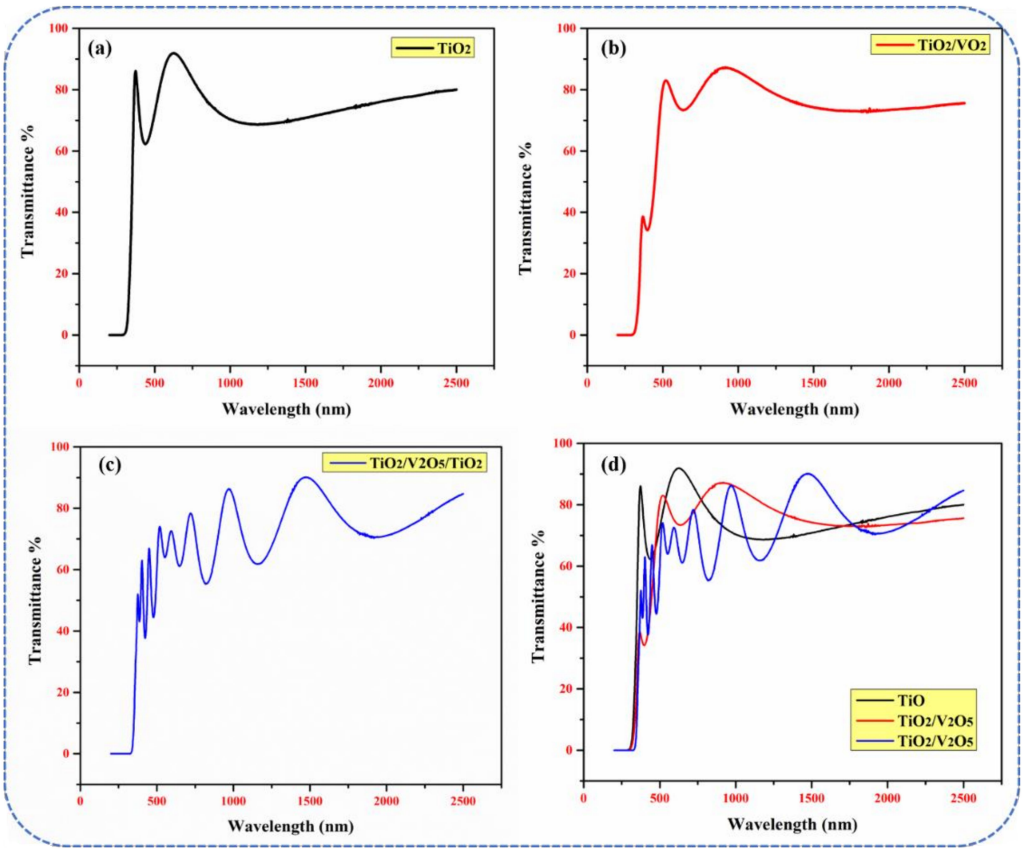

Figure 3. Transmittance spectra of (**a**) single-layer TiO_2, (**b**) bi-layer TiO_2/V_2O_5, and (**c**) multi-layer $TiO_2/V_2O_5/TiO_2$ thin films; (**d**) the combination of spectra for the mono-, bi-, and multi-layer thin films, respectively.

The optical absorption coefficient (α) was plotted as a function of photon energy ($h\nu$) and the spectra are shown in Figure 4a–c. Tauc's plot was used to determine the optical bandgap (E_{BG}) of the thin films. In the mono-layer, a typical E_{BG} ~ 3.49 eV for the anatase TiO_2 (Figure 4a) was obtained [38]. Two E_{BG} values were observed in the bi-layer, which are attributable to the anatase TiO_2 (E_{BG} ~ 3.50 eV) and α-V_2O_5 (E_{BG} ~ 1.93 eV), as shown in Figure 4b. The stoichiometry of V_2O_5 indicates that E_{BG} ~ 2.6 eV. Here, the decreased E_{BG} is due to the non-stoichiometry, oxide network, nanoporosity, and lower thickness of the V_2O_5 layer [39]. In the tri-layer, a single value of E_{BG} ~ 3.51 eV was observed in Figure 4c. The diffused E_{BG} is attributed to the inter-diffusion of the different layers during the deposition at relatively high substrate temperatures.

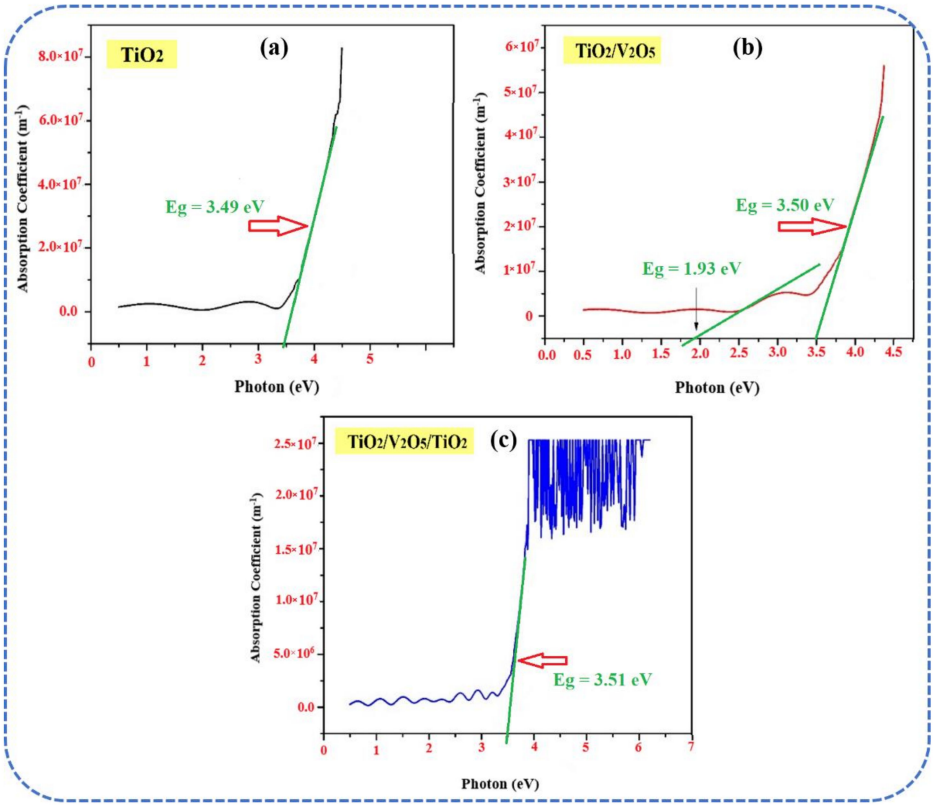

Figure 4. Plots of the optical absorption coefficient (α) vs. photon energy (hν) for (**a**) TiO_2, (**b**) bi-layer TiO_2/V_2O_5, and (**c**) multi-layer $TiO_2/V_2O_5/TiO_2$ thin films.

Lastly, the resistivity of the mono-, bi-, and tri-layers is shown in Figure 5. First, the resistance was determined from the current (I) and potential (V). Subsequently, the resistivity was calculated by multiplying the resistance with the thickness (t) of the thin films. The conductivity was determined by taking the inverse of the resistivity, and the values are summarized in Table 2.

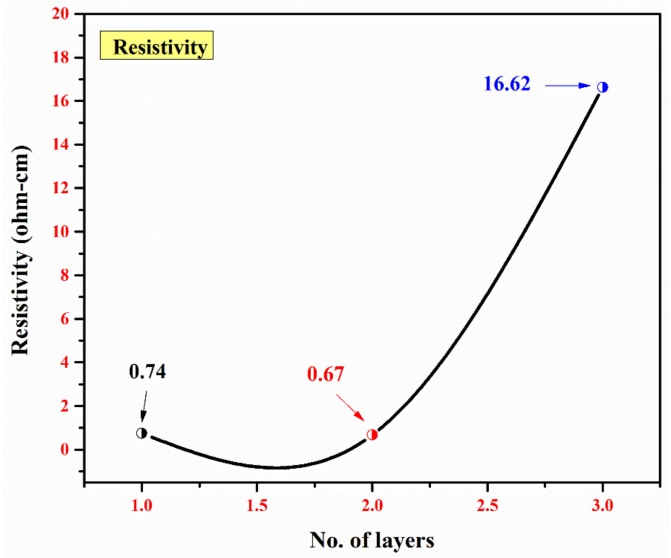

Figure 5. A plot of the no. of layers vs. resistivity (Ω-cm) for a single layer of TiO_2, a bi-layer of TiO_2/V_2O_5, and a multi-layer of $TiO_2/V_2O_5/TiO_2$.

Table 2. Resistance, resistivity, and conductivity of the mono-, bi-, and tri-layers.

Samples	Resistance (Ω)	Resistivity (Ω-cm)	Conductivity $(\Omega\text{-cm})^{-1}$
mono-layer (TiO_2)	504×10^6	0.74	1.35
bi-layer (TiO_2/V_2O_5)	336×10^6	0.67	1.48
tri-layer ($TiO_2/V_2O_5/TiO_2$)	541×10^7	16.62	0.06

The resistivity of 0.74 Ω-cm was obtained in the mono-layer. A decrease in resistivity to 0.67 Ω-cm was observed in the bi-layer. Considering the optimal stoichiometry, the resistivity of a particular material depends on its morphological and structural parameters (e.g., thickness, phase composition, and dimensions). Bulk V_2O_5 has a resistivity of 2.1×10^7 Ω-cm. As reported [40], a decrease in resistivity was observed for V_2O_5 thin films as their thicknesses were decreased, i.e., 8.7×10^6 Ω-cm for 85 nm-thick films and 2.14×10^7 Ω-cm for 112 nm-thick films. In the presented work, a substantial decrease in resistivity was observed and the reason for this is two-fold: (i) a relatively thin V_2O_5 layer (approx. 50 nm thick) and (ii) the TiO_2/V_2O_5 interface. Moreover, the oxygen deficiency in the bi-layer resulted in an increase in the conductivity (1.48 Ω^{-1}-cm^{-1} for the bi-layer compared to 1.35 Ω^{-1}-cm^{-1} for the mono-layer). For the tri-layer, the conductivity decreased to 0.06 Ω^{-1}-cm^{-1} due to the relatively thick top TiO_2 layer (360 nm).

4. Conclusions

Smooth and uniform nanocomposite $TiO_2/V_2O_5/TiO_2$ multi-layer thin films were prepared as a solar water heater device using the electron beam evaporation technique. The total thickness of the SWHD thin film was approx. 600 nm on a 1 mm-thick transparent soda–lime glass substrate. The RBS and SEM analyses confirmed the successful formation of a nanocomposite multi-layered structure at the nanoscale level with optimal stoichiometry. The optical transmittance of the TiO_2 mono-layer was ~92% in the visible region. In the TiO_2/V_2O_5 bi-layer, the optical transmittance decreased to ~82% due to the increased total thickness (approx. 200 nm) compared to that of the mono-layer (150 nm) and due to the increased absorption of the incident light by V_2O_5. Nevertheless, the bi-layer possessed good transparency in the infrared region, contrary to the mono-layer. In the case of the $TiO_2/V_2O_5/TiO_2$ tri-layer, transmittances of ~78% in the visible and ~90% in the infrared regions were observed due to the increased total thickness of the thin film (approx. 600 nm) and multiple photon reflections between the constituent layers. An optical bandgap of approx. 3.5 eV was determined for the SWHD (tri-layer) with a high conductivity (resistivity of approx. 16.6 Ω-cm).

Author Contributions: Conceptualization, A.F.K.; methodology, I.R., M.B.H. and M.M.; software, A.F.K.; validation, M.M., I.R. and M.B.H.; formal analysis, I.R. and M.B.H.; investigation, I.R. and A.F.K.; resources, A.F.K.; data curation, I.R.; writing—original draft preparation, I.R., M.B.H., M.M., A.F.K., A.S.A., K.S.A.H., A.K. and T.S.; writing—review and editing, I.R., M.B.H., M.M., A.F.K., A.S.A., K.S.A.H., A.K. and T.S.; visualization, A.F.K., M.M. and T.S.; supervision, A.F.K.; project administration, A.F.K. and M.M.; funding acquisition, A.F.K. and T.S. All authors have read and agreed to the published version of the manuscript.

Funding: This research has been funded by the Scientific Research Deanship at the University of Ha'il—Saudi Arabia through project number RG-21 092.

Institutional Review Board Statement: Not applicable.

Informed Consent Statement: Not applicable.

Data Availability Statement: The data presented in this study are available on request from the corresponding author.

Conflicts of Interest: The authors declare no conflict of interest. The funders had no role in the design of the study; in the collection, analysis, or interpretation of data; in the writing of the manuscript; or in the decision to publish the results.

References

1. Liu, J.; Wang, F.; Zhang, L.; Fang, X.; Zhang, Z. Thermodynamic properties and thermal stability of ionic liquid-based nanofluids containing graphene as advanced heat transfer fluids for medium-to-high-temperature applications. *Renew. Energy* **2014**, *63*, 519–523. [CrossRef]
2. Lan, F.; Jiang, M.; Tao, Q.; Li, G. Revealing the working mechanisms of planar perovskite solar cells with cross-sectional surface potential profiling. *IEEE J. Photovolt.* **2017**, *8*, 125–131. [CrossRef]
3. Sharma, A.; Chen, C.R.; Lan, N.V. Solar-energy drying systems: A review. *Renew. Sustain. Energy Rev.* **2009**, *13*, 1185–1210. [CrossRef]
4. Ziabari, A.A.; Khatibani, A.B. Optical properties and thermal stability of solar selective absorbers based on Co-Al_2O_3 cermets. *Chin. J. Phys.* **2017**, *55*, 876–885. [CrossRef]
5. Lin, K.T.; Lin, H.; Yang, T.; Jia, B. Structured graphene metamaterial selective absorbers for high efficiency and omnidirectional solar thermal energy conversion. *Nat. Commun.* **2020**, *11*, 1389. [CrossRef]
6. Goel, N.; Taylor, R.A.; Otanicar, T. A review of nanofluid-based direct absorption solar collectors: Design considerations and experiments with hybrid PV/Thermal and direct steam generation collectors. *Renew. Energy* **2020**, *145*, 903–913. [CrossRef]
7. Chen, C.; Yang, C.; Ranjan, D.; Loutzenhiser, P.G.; Zhang, Z.M. Spectral radiative properties of ceramic particles for concentrated solar thermal energy storage applications. *Int. J. Thermophys.* **2020**, *41*, 152. [CrossRef]
8. Chang, C.C.; Chi, P.W.; Chandan, P.; Lin, C.K. Electrochemistry and rapid electrochromism control of MoO_3/V_2O_5 hybrid nanobilayers. *Materials* **2019**, *12*, 2475. [CrossRef]
9. Surca, A.K.; Dražić, G.; Mihelčič, M. Low-temperature V-oxide film for a flexible electrochromic device: Comparison of its electrochromic, IR and Raman properties to those of a crystalline V_2O_5 film. *Sol. Energy Mater. Sol. Cells* **2019**, *196*, 185–199. [CrossRef]
10. Mjejri, I.; Gaudon, M.; Rougier, A. Mo addition for improved electrochromic properties of V_2O_5 thick films. *Sol. Energy Mater. Sol. Cells* **2019**, *198*, 19–25. [CrossRef]
11. Dalavi, D.S.; Bhosale, A.K.; Desai, R.S.; Patil, P.S. Energy efficient electrochromic smart windows based on highly stable CeO_2-V_2O_5 optically passive counter electrode. *Mater. Today Proc.* **2021**, *43*, 2702–2706. [CrossRef]
12. Jain, R.K.; Khanna, A. Structural, optical and electrical properties of crystalline V_2O_5 films deposited by thermal evaporation and effects of temperature on UV–vis and Raman spectra. *Optik* **2017**, *144*, 271–280. [CrossRef]
13. Mukherjee, A.; Sa, N.; Phillips, P.J.; Burrell, A.; Vaughey, J.; Klie, R.F. Direct investigation of Mg intercalation into the orthorhombic V_2O_5 cathode using atomic-resolution transmission electron microscopy. *Chem. Mater.* **2017**, *29*, 2218–2226. [CrossRef]
14. Peng, C.; Li, Y.; Wu, Y.; Zhang, X.; Zou, M.; Zhuang, J.; Wang, X. Electrical and optical properties of W-doped V_2O_5/FTO composite films fabricated by sol–gel method. *Infrared Phys. Technol.* **2021**, *116*, 103807. [CrossRef]
15. Kang, M.; Kim, S.W.; Park, H.Y. Optical properties of TiO_2 thin films with crystal structure. *J. Phys. Chem. Solids* **2018**, *123*, 266–270. [CrossRef]
16. Etemadi, B.; Mazloom, J.; Ghodsi, F.E. Phase transition and surface morphology effects on optical, electrical and lithiation/delithiation behavior of nanostructured Ce-doped V_2O_5 thin films. *Mater. Sci. Semicond. Processing* **2017**, *61*, 99–106. [CrossRef]
17. Ahmadi, K.; Ziabari, A.A.; Mirabbaszadeh, K.; Shal, A.A. Synthesis and characterization of ZnO/TiO_2 composite core/shell nanorod arrays by sol–gel method for organic solar cell applications. *Bull. Mater. Sci.* **2015**, *38*, 617–623. [CrossRef]
18. Liu, T.; Liu, B.; Wang, J.; Yang, L.; Ma, X.; Li, H.; Wang, Y. Smart window coating based on F-TiO_2-K_xWO_3 nanocomposites with heat shielding, ultraviolet isolating, hydrophilic and photocatalytic performance. *Sci. Rep.* **2016**, *6*, 27373. [CrossRef]
19. Patil, R.A.; Devan, R.S.; Liou, Y.; Ma, Y.R. Efficient electrochromic smart windows of one-dimensional pure brookite TiO_2 nanoneedles. *Sol. Energy Mater. Sol. Cells* **2016**, *147*, 240–245. [CrossRef]
20. Karbalaei Akbari, M.; Zhuiykov, S. A bioinspired optoelectronically engineered artificial neurorobotics device with sensorimotor functionalities. *Nat. Commun.* **2019**, *10*, 3873. [CrossRef]
21. Myung, S.T.; Kikuchi, M.; Yoon, C.S.; Yashiro, H.; Kim, S.J.; Sun, Y.K.; Scrosati, B. Black anatase titania enabling ultra high cycling rates for rechargeable lithium batteries. *Energy Environ. Sci.* **2013**, *6*, 2609–2614. [CrossRef]
22. Haider, A.J.; Jameel, Z.N.; Al-Hussaini, I.H. Review on: Titanium dioxide applications. *Energy Procedia* **2019**, *157*, 17–29. [CrossRef]
23. Mohamed, H.A. Sintering process and annealing effect on some physical properties of V_2O_5 thin films. *Optoelectron. Adv. Mater.-Rapid Commun.* **2009**, *3*, 693–699.
24. Al-Kuhaili, M.F.; Khawaja, E.E.; Ingram, D.C.; Durrani, S.M.A. A study of thin films of V_2O_5 containing molybdenum from an evaporation boat. *Thin Solid Film.* **2004**, *460*, 30–35. [CrossRef]
25. Ramana, C.V.; Hussain, O.M.; Naidu, B.S.; Julien, C.; Balkanski, M. Physical investigations on electron-beam evaporated vanadium pentoxide films. *Mater. Sci. Eng. B* **1998**, *52*, 32–39. [CrossRef]
26. Sheng, Y.; Yang, J.; Wang, F.; Liu, L.; Liu, H.; Yan, C.; Guo, Z. Sol-gel synthesized hexagonal boron nitride/titania nanocomposites with enhanced photocatalytic activity. *Appl. Surf. Sci.* **2019**, *465*, 154–163. [CrossRef]

27. Kim, S.; Kim, M.; Lim, S.K.; Park, Y. Titania-coated plastic optical fiber fabrics for remote photocatalytic degradation of aqueous pollutants. *J. Environ. Chem. Eng.* **2017**, *5*, 1899–1905. [CrossRef]
28. Fu, Y.; Mo, A. A review on the electrochemically self-organized titania nanotube arrays: Synthesis, modifications, and biomedical applications. *Nanoscale Res. Lett.* **2018**, *13*, 187. [CrossRef]
29. Khan, M.I.; Arfan, M.; Farooq, W.A.; Shehzad, A.; Saleem, M.; Fatima, M.; Iqbal, M. Improved photovoltaic performance of dye-sensitized solar cells by Au-ion implantation of titania film electrodes. *Results Phys.* **2020**, *17*, 103093. [CrossRef]
30. Chen, H.W.; Hong, C.Y.; Kung, C.W.; Mou, C.Y.; Wu, K.C.W.; Ho, K.C. A gold surface plasmon enhanced mesoporous titanium dioxide photoelectrode for the plastic-based flexible dye-sensitized solar cells. *J. Power Sources* **2015**, *288*, 221–228. [CrossRef]
31. Zhou, C.; Xi, Z.; Stacchiola, D.J.; Liu, M. Application of ultrathin TiO_2 layers in solar energy conversion devices. *Energy Sci. Eng.* **2022**, *10*, 1614–1629. [CrossRef]
32. Nawade, A.; Ramya, K.; Chakrabortty, S.; Bamola, P.; Sharma, H.; Sharma, M.; Dalapati, G.K. Copper based transparent solar heat rejecting film on glass through in-situ nanocrystal engineering of sputtered TiO_2. *Ceram. Int.* **2022**, *48*, 2482–2491. [CrossRef]
33. Fikri, M.A.; Faizal, W.M.; Adli, H.K.; Mamat, R.; Azmi, W.H.; Majid, Z.A.A.; Ramadhan, A.I. Characteristic of TiO_2-SiO_2 Nanofluid with Water/Ethylene Glycol Mixture for Solar Application. *J. Adv. Res. Fluid Mech. Therm. Sci.* **2021**, *81*, 113. [CrossRef]
34. Abrar, S.; Hanif, M.B.; Alghamdi, A.S.; Khaliq, A.; Abdel Halim, K.S.; Subhani, T.; Motola, M.; Khan, A.F. Synthesis and Characterization of Nanostructured Multi-Layer Cr/SnO_2/NiO/Cr Coatings Prepared via E-Beam Evaporation Technique for Metal-Insulator-Insulator-Metal Diodes. *Materials* **2022**, *15*, 3906. [CrossRef]
35. Hanif, M.B.; Motola, M.; Qayyum, S.; Rauf, S.; Khalid, A.; Li, C.-J.; Li, C.-X. Recent advancements, doping strategies, and the future perspective of perovskite-based Solid oxide fuel cells for energy conversion. *Chem. Eng. J.* **2022**, *428*, 132603. [CrossRef]
36. Hanif, M.B.; Rauf, S.; Motola, M.; Babar, Z.U.D.; Li, C.-J.; Li, C.-X. Recent progress of perovskite-based electrolyte materials for solid oxide fuel cells and performance optimizing strategies for energy storage applications. *Mater. Res. Bull.* **2022**, *146*, 111612. [CrossRef]
37. Babar, Z.U.D.; Hanif, M.B.; Gao, J.T.; Li, C.J.; Li, C.X. Sintering behavior of $BaCe_{0.7}Zr_{0.1}Y_{0.2}O_{3-\delta}$ electrolyte at 1150 °C with the utilization of CuO and Bi_2O_3 as sintering aids and its electrical performance. *Int. J. Hydrogen Energy* **2022**, *47*, 7403–7414. [CrossRef]
38. Cheema, D.A.; Danial, M.O.; Hanif, M.B.; Alghamdi, A.S.; Ramadan, M.; Khaliq, A.; Khan, A.F.; Subhani, T.; Motola, M. Intrinsic Properties and Future Perspective of HfO_2/V_2O_2/HfO_2 Multi-Layer Thin Films via E-Beam Evaporation as a Transparent Heat Mirror. *Coatings* **2022**, *12*, 448. [CrossRef]
39. Hanif, M.B.; Gao, J.T.; Shaheen, K.; Wang, Y.P.; Yasir, M.; Zhang, S.L.; Li, C.J.; Li, C.X. Performance evaluation of highly active and novel $La_{0.7}Sr_{0.3}Ti_{0.1}Fe_{0.6}Ni_{0.3}O_{3-\delta}$ material both as cathode and anode for intermediate-temperature symmetrical solid oxide fuel cell. *J. Power Sources* **2020**, *472*, 228498. [CrossRef]
40. Motola, M.; Hromadko, L.; Prikryl, J.; Sopha, H.; Krbal, M.; Macak, J.M. Intrinsic properties of high-aspect ratio single-and double-wall anodic TiO_2 nanotube layers annealed at different temperatures. *Electrochim. Acta* **2020**, *352*, 136479. [CrossRef]
41. Saleem, M.S.; Hanif, M.B.; Gregor, M.; Motola, M.; Khan, A.F. Nanostructured multi-layer MgF_2/ITO coatings prepared via e-beam evaporation for efficient electromagnetic interference shielding performance. *Appl. Surf. Sci.* **2022**, *11*, 153584. [CrossRef]
42. Motola, M.; Capek, J.; Zazpe, R.; Bacova, J.; Hromadko, L.; Bruckova, L.; Macak, J.M. Thin TiO_2 coatings by ALD enhance the cell growth on TiO_2 nanotubular and flat substrates. *ACS Appl. Bio Mater.* **2020**, *3*, 6447–6456. [CrossRef]
43. Motola, M.; Dworniczek, E.; Satrapinskyy, L.; Chodaczek, G.; Grzesiak, J.; Gregor, M.; Plesch, G. UV light-induced photocatalytic, antimicrobial, and antibiofilm performance of anodic TiO_2 nanotube layers prepared on titanium mesh and Ti sputtered on silicon. *Chem. Pap.* **2019**, *73*, 1163–1172. [CrossRef]
44. Nkele, A.C.; Chime, U.K.; Asogwa, L.; Nwanya, A.C.; Nwankwo, U.; Ukoba, K.; Ezema, F.I. A study on titanium dioxide nanoparticles synthesized from titanium isopropoxide under SILAR-induced gel method: Transition from anatase to rutile structure. *Inorg. Chem. Commun.* **2020**, *112*, 107705. [CrossRef]
45. Li, W.; Luo, X.; Yang, P.; Wang, Q.; Zeng, M.; Markides, C.N. Solar-thermal energy conversion prediction of building envelope using thermochemical sorbent based on established reaction kinetics. *Energy Convers. Manag.* **2022**, *252*, 115117. [CrossRef]
46. Liu, X.; Chen, M.; Xu, Q.; Gao, K.; Dang, C.; Li, P.; Ding, Y. Bamboo derived SiC ceramics-phase change composites for efficient, rapid, and compact solar thermal energy storage. *Sol. Energy Mater. Sol. Cells* **2022**, *240*, 111726. [CrossRef]
47. Paine, D.C.; Whitson, T.; Janiac, D.; Beresford, R.; Yang, C.O.; Lewis, B. A study of low temperature crystallization of amorphous thin film indium–tin–oxide. *J. Appl. Phys.* **1999**, *85*, 8445–8450. [CrossRef]
48. Chain, E.E. Optical properties of vanadium dioxide and vanadium pentoxide thin films. *Appl. Opt.* **1991**, *30*, 2782–2787. [CrossRef]
49. Ahmadi, K.; Ziabari, A.A.; Mirabbaszadeh, K.; Ahmadi, S. Synthesis of TiO_2 nanotube array thin films and determination of the optical constants using transmittance data. *Superlattices Microstruct.* **2015**, *77*, 25–34. [CrossRef]
50. Basu, R.; Prasad, A.K.; Dhara, S.; Das, A. Role of vanadyl oxygen in understanding metallic behavior of V_2O_5 (001) nanorods. *J. Phys. Chem. C* **2016**, *120*, 26539–26543. [CrossRef]
51. Akl, A.A. Crystallization and electrical properties of V_2O_5 thin films prepared by RF sputtering. *Appl. Surf. Sci.* **2007**, *253*, 7094–7099. [CrossRef]
52. Pore, V.; Rahtu, A.; Leskelä, M.; Ritala, M.; Sajavaara, T.; Keinonen, J. Atomic layer deposition of photocatalytic TiO_2 thin films from titanium tetramethoxide and water. *Chem. Vap. Depos.* **2004**, *10*, 143–148. [CrossRef]